

Review

# Research Progress on Femtosecond Laser Poling of Ferroelectrics

Yan Sheng <sup>1,2,\*</sup>, Xin Chen <sup>3,4</sup> , Tianxiang Xu <sup>1,2</sup> , Shan Liu <sup>5</sup>, Ruwei Zhao <sup>1,2</sup> and Wieslaw Krolikowski <sup>5</sup>

<sup>1</sup> Laboratory of Infrared Materials and Devices, Research Institute of Advanced Technologies, Ningbo University, Ningbo 315211, China

<sup>2</sup> Zhejiang Key Laboratory of Advanced Optical Functional Materials and Devices, Ningbo University, Ningbo 315211, China

<sup>3</sup> Department of Optical Information Science and Technology, School of Physics, Xidian University, Xi'an 710071, China

<sup>4</sup> Guangzhou Institute of Technology, Xidian University, Guangzhou 510555, China

<sup>5</sup> Quantum Science and Technology, Research School of Physics, Australian National University, Canberra, ACT 2601, Australia

\* Correspondence: shengyan@nbu.edu.cn

**Abstract:** Ferroelectric domain engineering has wide applications in optical and electronic industries. Compared with traditional electric field poling, femtosecond laser poling has many advantages, such as higher fabrication resolution, 3D engineering applicability, and lower costs of production. In this review, the recent research progress on ferroelectric domain engineering with femtosecond laser pulses is presented. We show the latest results, including complex domain structures fabricated in various kinds of ferroelectric crystals, and discuss the influence of laser poling parameters and conditions on the morphologies of inverted domains and their physical mechanisms. The technical challenges to overcome in future are also briefly discussed.

**Keywords:** ferroelectric domain engineering; quasi-phase matching; laser frequency conversion



**Citation:** Sheng, Y.; Chen, X.; Xu, T.; Liu, S.; Zhao, R.; Krolikowski, W. Research Progress on Femtosecond Laser Poling of Ferroelectrics.

*Photonics* **2024**, *11*, 447.

<https://doi.org/10.3390/photonics11050447>

Received: 9 April 2024

Revised: 30 April 2024

Accepted: 6 May 2024

Published: 10 May 2024



**Copyright:** © 2024 by the authors. Licensee MDPI, Basel, Switzerland. This article is an open access article distributed under the terms and conditions of the Creative Commons Attribution (CC BY) license (<https://creativecommons.org/licenses/by/4.0/>).

## 1. Introduction

In the 1980s, a crucial technological breakthrough happened in the field of material processing, owing to the emergence of the ultra-fast femtosecond laser. Femtosecond laser direct writing, i.e., the localized modification of a material's properties with light, provides several advantages over traditional techniques. The first one is the extremely high precision of fabrication. The rate of energy deposition induced by a femtosecond laser is faster than the rate of thermal diffusion (usually  $10^{-12}$  s scale), thus leaving the surrounding material unaffected and ensuring a higher processing precision. In addition, tightly focused femtosecond pulses can induce two-/multi-photon processes, such as multi-photon absorption, to break the diffraction limit and achieve sub-wavelength resolution. Secondly, femtosecond laser writing is capable of fabricating three-dimensional (3D) structures by focusing and scanning the beam inside the volume of transparent materials, a unique capability that makes it an irreplaceable processing tool. The third is the versatility in aspects of its application scope and the resulting functionalities. The femtosecond laser-induced structures depend mainly on the characteristics of the atomic structure of the material and the laser pulses, especially the pulse peak intensity. The ultrashort pulse duration ( $10^{-15}$  s) and ultrahigh peak intensity ( $10^{15}$  W/cm<sup>2</sup>) lead to a low restriction on processable material categories. On the other hand, depending on the laser's parameters, the underlying light-matter interaction mechanisms can be different. Therefore, plentiful processing effects can be obtained with a femtosecond laser direct writing technique. So far, sophisticated structures and devices with different functionalities fabricated with femtosecond laser pulses have been widely used in areas including fundamental physics, material science, biology, and medicine [1–9].

One important application of femtosecond laser writing is in the fabrication of micro/nano optical devices. For instance, the process can be used to integrate various optical components, including waveguides, Bragg gratings, couplers, mirrors, lenses, etc., on the surface or inside optical fibers with zero pollution. The so-called lab-on-fibers and lab-in-fibers can greatly improve the performance of optical fibers owing to robustness, flexibility, and versatility [10–13]. The realization of these optical devices is all based on the modulation of the linear optical properties of the materials.

As for the modulation of nonlinear optical properties, especially second order nonlinearity, femtosecond laser writing has only recently been experimentally demonstrated as a powerful technique, although the idea was proposed in the 1990s [14]. In ferroelectric materials, spatial modulation of the second order nonlinear susceptibility tensor  $\chi^{(2)}$  corresponds to the modulation of the spontaneous polarization and formation of localized ferroelectric domains. This can be obtained by applying, e.g., a periodic external electric field to the material. Major applications of ferroelectric domain structures created in this way include nonlinear optical frequency conversion. Artificial structures with a spatially modulated  $\chi^{(2)}$  but a constant refractive index are known as nonlinear photonic crystals (NPCs) [15]. As the core element of so-called quasi-phase matching (QPM) [16], NPCs can be used to compensate for the phase mismatch between interacting waves by providing the required reciprocal lattice vectors (RLVs), which enable the efficient generation and manipulation of light at new frequencies [17,18].

Normally, the switching of spontaneous polarization or ferroelectric domain inversion is realized by applying an electric field that is larger than the coercive field ( $E_c$ ). Through patterned electrodes, spatially varying and, in particular, periodic ferroelectric domain structures can be created to form artificial structures like NPCs. Although the electric field poling (EFP) method has been utilized as the main technique for fabricating NPCs since the 1990s [19], it suffers from several disadvantages. The main one is the inability to fabricate three-dimensional (3D) ferroelectric domains, which severely limits the functionality and performance of devices like NPCs and ferroelectric random-access memories [20]. For instance, 3D NPCs can provide much more abundant RLVs with different magnitudes and orientations, thus capable of compensating for phase mismatches in complicated nonlinear optical processes that are inaccessible with lower dimensional NPCs [21]. EFP is also an inflexible technique for fabricating non-polar cuts in NPCs, which are more favorable for certain applications. For instance,  $x$ -cut lithium niobate ( $\text{LiNbO}_3$ ) is commonly used in electro-optic modulators. To electrically pole an  $x$ -cut  $\text{LiNbO}_3$  usually requires finger electrodes, which not only increases the processing difficulty in fabricating 2D NPCs but also limits the resolution of domain patterning. Moreover, EFP cannot be used to pole thick crystals without dielectric breakdown.

To overcome the disadvantages of EFP, different techniques have been developed. For instance, poling with an atomic force microscope (AFM) probe tip and electron beam poling can remove the restrictions of patterned electrodes, making them flexible enough to create pattern domains with submicron details [22–24]. However, this approach still does not allow the creation of 3D poling, and it is impractical for large-scale fabrications.

Laser direct writing is naturally advantageous in fabricating 3D microstructures with high resolutions. Optical poling without electric contacts is also a noninvasive method that offers favorable characteristics for next-generation all-optical networks [25–27]. In the last decade, tremendous efforts have been devoted to inverting ferroelectric domains using laser beams at different wavelengths. Initially, it was found that weak absorption of laser light could reduce the coercive field  $E_c$  of ferroelectric crystals. This effect was used to define domain patterns by first selectively irradiating the ferroelectric crystal with a laser beam, then applying a homogeneous electric field to create domain inversions at irradiated areas. Although this so-called light-assisted poling (LAP) eliminates the need for patterned electrodes, inverted domains are still restricted to low-dimensional (1D and 2D) structures in polar-cut crystals [28]. Afterwards, UV lasers were extensively investigated for potential usefulness in non-polar facets poling at submicron poling resolutions [29–33]. However,

as most ferroelectric crystals are highly absorptive in the UV range, the inverted domains are restricted to a very shallow surface (less than a few microns) and often accompanied by optical damage [30]. A CO<sub>2</sub> laser at 10.6 μm was also used for direct laser poling. Although the depth of the inverted domains (tens of micrometers) is greatly increased when compared with UV poling, this approach requires a mask to achieve periodic domain structures [34,35]. Otherwise, the obtained so-called self-similar or self-organized domain patterns usually consist of intense nanodomain rays, which cannot be controlled using light illumination.

Finally, in 2018, a breakthrough in 3D poling was achieved using femtosecond laser pulses [36]. This all-optical poling method utilizes near-infrared pulses and the multiphoton absorption of light to create a thermoelectric field through a light-induced temperature gradient to directly reverse ferroelectric domains under the proper conditions. It can achieve 3D poling by focusing the laser beam at different depths, making use of the high linear transmittance of ferroelectric crystals at 800 nm. The near-infrared method has been used for 1D, 2D, and 3D poling in a variety of ferroelectric crystals for nonlinear optical applications, including efficient frequency conversion, nonlinear holography, and nonlinear beam shaping [36–43].

In this review, we present an overview of near-infrared femtosecond laser-induced domain engineering in various ferroelectric crystals. We aim to provide a better understanding of domain inversions based on laser writing, thus stimulating the advancement of domain-engineered photonics. We will begin by discussing the basic features of ferroelectrics and the applications of ferroelectric domain structures. Then, in the “Ferroelectric Domain Visualization” section, we will list the techniques of ferroelectric domain visualization. The research progress on laser poling is presented in the next few sections, with an emphasis on the influences of laser poling parameters and the physical mechanisms being discussed. It should be noted that this review focuses on domain inversion techniques related to laser writing without applying external electric fields. Therefore, other  $\chi^{(2)}$  engineering techniques like LAP (for which an electric field is required) and the laser  $\chi^{(2)}$  erasing approach (not domain inversion) are not discussed here. One can refer to references [44–46] for works on LAP and the laser  $\chi^{(2)}$  erasing approach.

## 2. Basics and Applications of Ferroelectric Domain Structures

Ferroelectric domain inversion leads to reversed signing of all odd-order tensors of the material's physical quantities, (e.g., the aforementioned quadratic nonlinear tensor  $\chi^{(2)}$  and the piezoelectric tensor), while keeping all even-order tensors unchanged (e.g., the thermoelectric power tensor, second rank). Apart from the important applications in nonlinear optics mentioned above, ferroelectric domain inversion is also useful in many other fields. For instance, microstructures with periodical modulations of the piezoelectric tensor are known as piezoelectric phononic crystals or acoustic superlattices. Unlike a pure elastic phononic crystal, which usually consists of materials with different elastic moduli and/or mass densities, a domain inversion phononic crystal is a monolithic crystal that is attractive for applications involving generating, detecting, and manipulating surface acoustic waves [47–49]. In addition, antiparallel ferroelectric domains can be treated as binary states, which forms a basis for various applications. For instance, the domain orientation is used to store information and the domain inversion current is used to read out the stored information [20]. Another example is a tunnel junction with a ferroelectric barrier, where domain inversion can be used to obtain continuous tuning of the tunnel resistance between the on and off statuses. This behavior is expected to open a new frontier in neuromorphic computational architectures [50]. On the other hand, studies show that ferroelectric domain walls, which separate regions with different orientations of spontaneous polarizations, possess additional functionalities (e.g., conductivity or even superconductivity) comparing favorably with the host materials [51,52]. Consequently, switching the ferroelectric domains and manipulating the domain walls provide promising paradigms for realizing next-generation ferroelectric devices.

$\text{LiNbO}_3$  is one of the most used materials in optically induced ferroelectric domain inversion not only because of its outstanding optical properties such as a broad transmission window and large nonlinear susceptibility, but also because of its wide availability. High quality single-domain LN wafers are commercially available in sizes up to 300 mm (11.8 inches) in diameter. In addition, thin-film LN on insulator wafers (LNOI), which possess a large refractive index contrast and a small bending radius, have been developed into a promising platform for use in devices that require high efficiency and low power consumption [53–56].

Apart from single-domain crystals, multi-domain crystals, including barium calcium titanate ( $\text{Ba}_x\text{Ca}_{1-x}\text{TiO}_3$ , BCT), calcium barium niobate ( $\text{Ca}_x\text{Ba}_{1-x}\text{Nb}_2\text{O}_6$ , CBN), and strontium barium niobate ( $\text{Sr}_x\text{Ba}_{1-x}\text{Nb}_2\text{O}_6$ , SBN) crystals have also been used in optical poling experiments. Compared with  $\text{LiNbO}_3$ , the  $E_c$  of BCT, SBN, and CBN crystals is much lower. The first artificially patterned 3D domain structure was experimentally demonstrated in an  $x$ -cut BCT crystal [36]. By focusing near-infrared laser pulses inside  $180^\circ$  random domain areas, the originally nano-sized domains are locally realigned and merged into a theta-shaped domain consisting of two large single domains with opposite directions of spontaneous polarization. However, the  $90^\circ$  domain walls in BCT are detrimental to applications due to their scattering loss. Later on, 3D poling was also demonstrated in SBN and CBN crystals, which contain only  $180^\circ$  domains [40,42].

At room temperature, the multi-domain crystal possesses randomly distributed domains with specific orientations and sizes. For instance, as-grown CBN and SBN crystals feature random distributions of antiparallel  $180^\circ$  domains. These domains are needle-like, with lengths ranging from hundreds of nanometers to several micrometers (Figure 1). The irregularly distributed domains inside as-grown crystals can provide RLVs with random orientations and magnitudes (illustrated by the arrows in Figure 1), which can be used for broadband nonlinear interactions including second harmonic generation and cascaded third harmonic generations [57–60]. Compared with SBNs ( $T_c$  around  $75^\circ\text{C}$  for SBN-61), the Curie temperature of CBNs ( $T_c$  around  $265^\circ\text{C}$  or CBN-28) is much higher and thereby more suitable for applications involving high power lasers [58].

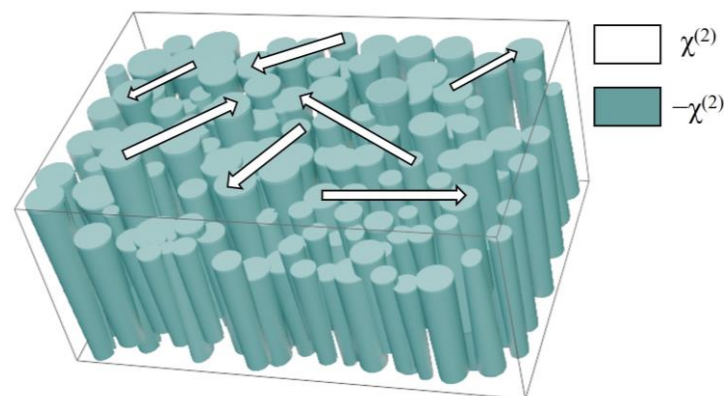


**Figure 1.** A schematic representation of the randomly distributed ferroelectric domains in as-grown ferroelectric crystals like SBNs and CBNs. The arrows stand for the reciprocal lattice vectors provided by the random domain structure.

To eliminate the scattering loss caused by random domain walls, multi-domain crystals can be converted into a single-domain state under certain conditions. For instance, single-domain CBN or tetragonal  $0.62\text{Pb}(\text{Mg}_{1/3}\text{Nb}_{2/3})\text{O}_3-0.38\text{PbTiO}_3$  (PMN-38PT) crystals can be obtained by applying a uniform electric field [61]. It was also demonstrated that 3D domain inversion can be realized in such single-domain CBN or PMN-38PT crystals [61,62]. As for crystals that contain more than one types of domain, such as crystals that possess both  $180^\circ$  and  $90^\circ$  domains, an annealing treatment is normally required to release strain and avoid cracking during the poling process [63].

### 3. Visualization of Ferroelectric Domains

The visualization of ferroelectric domains is indispensable because it not only provides experimental demonstration and characterization of the fabricated domain structures, but also gives us intuitive clues on the physical mechanism and dynamics of domain inversion, including the nucleation, growth, and merging of inverted domains. So far, different kinds of techniques have been established to image ferroelectric domain patterns after or even during the domain inversion process. It should be noted that antiparallel  $180^\circ$  domains are optically equal, so they cannot be directly imaged with the commonly used optical transmission or reflection microscopies.

Chemical etching is one of the most used domain visualization techniques. It works based on the different etching rates of positive and negative ends of ferroelectric dipoles in acids [64]. However, chemical etching is a destructive method and cannot be used to create a 3D visualization of ferroelectric domains.

Another commonly used domain visualization technique is piezo-response force microscopy (PFM) [65]. It relies on scanning the sample surface with a sharp conductive probe and applying an alternating current bias between the probe and the sample. By moving the probe over the sample surface and collecting and analyzing the deflection of the probe cantilever, the absolute orientation of the polarization of domains can be imaged. This is a nondestructive method and yields high resolutions of 5–10 nm. However, the 3D visualization of domain patterns is also beyond the capability of PFM.

To obtain 3D images of domain patterns, Cherenkov second harmonic microscopy can be used [66]. The imaging process is accomplished by detecting the Cherenkov second harmonic generated at places of differences in a ferroelectric crystal. The Cherenkov second harmonic generation is a noncollinear nonlinear process in which the second harmonic is emitted at the Cherenkov angle defined by the longitudinal phase matching condition [67]. The Cherenkov signal is strong when the incident laser beam illuminates areas where the second order nonlinear coefficient  $\chi^{(2)}$  undergoes abrupt spatial modulations, e.g., in the region of a domain wall. By contrast, the Cherenkov signal is almost absent when the laser beam illuminates a uniform domain. Thus, a 3D image of ferroelectric domain structures can be obtained by scanning the tightly focused fundamental beam in three dimensions and collecting the Cherenkov second harmonics signal emitted from each place. Cherenkov second harmonic microscopy has been demonstrated as a powerful imaging technique not only in a variety of ferroelectric crystals, but also in non-ferroelectric materials like orientation-patterned semiconductors [68]. In addition, this technique can be used for real-time in situ monitoring of ferroelectric kinetics during the poling and growth processes of domains [69]. The nucleation, growth, and lateral motion of domains visualized by Cherenkov second harmonic microscopy provide a deeper understanding of the domain inversion process.

The advantages and shortcomings of the domain visualization methods mentioned above are summarized in Table 1. Other domain visualization methods include confocal Raman microscopy (CRM), synchrotron X-ray scattering, time-resolved photoemission electron microscopy (PEEM), and in situ transmission electron microscopy (TEM) [70–73]. One can refer to references [74,75] for more details.

**Table 1.** Comparison of different methods of domain visualization.

Methods	High Resolution	Non-Destructive	3D Visualization
Chemical etching	Yes	No	No
Piezo-response force microscopy (PFM)	Yes	No	No
Cherenkov second harmonic microscopy	Yes	Yes	Yes

### 4. Physical Mechanism of Femtosecond Laser Poling

We will discuss the physical mechanism of laser poling using a multi-domain ( $180^\circ$  domains) crystal as an example [36]. It is well established that a domain inversion

with femtosecond pulses is caused by the laser-induced thermoelectric field inside ferroelectric materials. The nonlinear absorption of intense femtosecond laser pulses in the focal region induces a high temperature gradient (Figure 2a), which is the source of the thermoelectric field [76]. The temperature gradient has two opposite projections in the direction of the polar axis of the crystal (which is the direction of spontaneous polarization in the crystal, usually the  $z$  axis) (Figure 2b). Accordingly, the induced thermoelectric field (Figure 2c) is bipolar and forces the originally random  $180^\circ$  domains to reorient in the direction of this electric field and to form two large antiparallel domains (Figure 2d–f) in an  $x$ -cut BCT crystal [36]. Their visibly elongated profiles reflect the fact that for a cylindrically symmetric light intensity distribution in the focus, the  $z$  component of the induced thermoelectric field, which is responsible for poling, is asymmetric and drops faster in the direction normal to  $z$ , hence making the domains narrower in that direction.

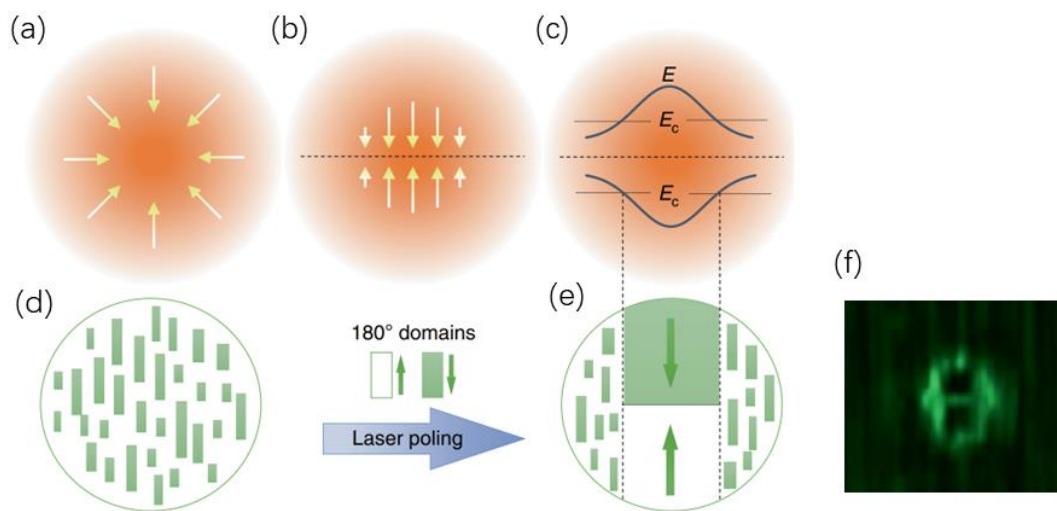


**Figure 2.** Schematic illustration of ferroelectric domain inversion with focused infrared femtosecond pulses [36]. (a) Nonlinear absorption of tightly focused pulses significantly increases the temperature, and its gradient in the focal area in the crystal (indicated by arrows) acts as a source of a thermoelectric field. (b) The change of the sign of the temperature gradient along the direction of spontaneous polarization. (c) The induced bipolar electric field and the formation of two larger antiparallel domains when the induced electric field exceeds the coercive field ( $E_c$ ) and, as shown in (d) (before poling), (e) (after poling), and (f) (The  $\theta$ -like domain structure created by femtosecond laser pulses, visualized by Cherenkov SH microscopy).

The thermoelectric field model discussed above can also be used to explain the sensitivity of domain inversion on the input surfaces in a monodomain  $\text{LiNbO}_3$  crystal. According to the model, the light-induced electric field can locally invert the domain if it is oriented opposite to the direction of spontaneous polarization and its strength exceeds the coercive field. Since the thermal profiles at  $-Z$  and  $+Z$  surfaces are exactly opposite, only the profile near the former surface results in a thermoelectric field oriented against the direction of spontaneous polarization and thus capable of domain inversion.

The femtosecond laser-induced thermoelectric field has been used to explain most of the experimental results on femtosecond laser poling so far. However, it is worth noting the femtosecond laser interaction with ferroelectric crystals is a rather complicated process that may involve many other physical effects like the pyroelectric effect, bulk screening, light-induced space charges, etc. The full understanding of light-induced ferroelectric domain inversion will require extensive studies in the future.

### 5. Femtosecond Laser Poling in Monodomain LiNbO<sub>3</sub> Crystal

The near-infrared laser-induced domain inversion in an LiNbO<sub>3</sub> crystal was experimentally demonstrated with a femtosecond oscillator (MIRA, Coherent, Saxonburg, PA, USA) operating at 800 nm [37]. The pulse duration and repetition rate were 180 fs and 76 MHz, respectively. The tightly focused laser beam was initially focused on the front (−Z) surface of the crystal. Then, the sample was translated along the Z-direction so that the position of the focal region moved from the −Z toward the Z surface with an average speed of  $v = 10 \mu\text{m/s}$ . As mentioned earlier, the femtosecond laser poling is sensitive to the crystal orientations. Specifically, domain inversion takes place only on the −Z surface in an LiNbO<sub>3</sub> crystal.

It has been found that the morphology of light-induced inverted domains depends critically on the laser power density in the irradiated region. Uniform and regular inverted domains can form only when the power density is high enough. This can be seen from Figure 3, which shows inverted domain structures obtained using microscope objectives of different numerical apertures (NAs). With low NAs (e.g., NA = 0.2 and 0.3), only randomly distributed domain islands could be formed (Figure 3a,b), even using the maximal incident power (700 mW) under our experimental condition permit. With a sufficiently strong laser power density, e.g., tightly focused using an NA = 0.65 objective, the inverted domains were precisely located in the irradiated positions, as shown in Figure 3c–h.

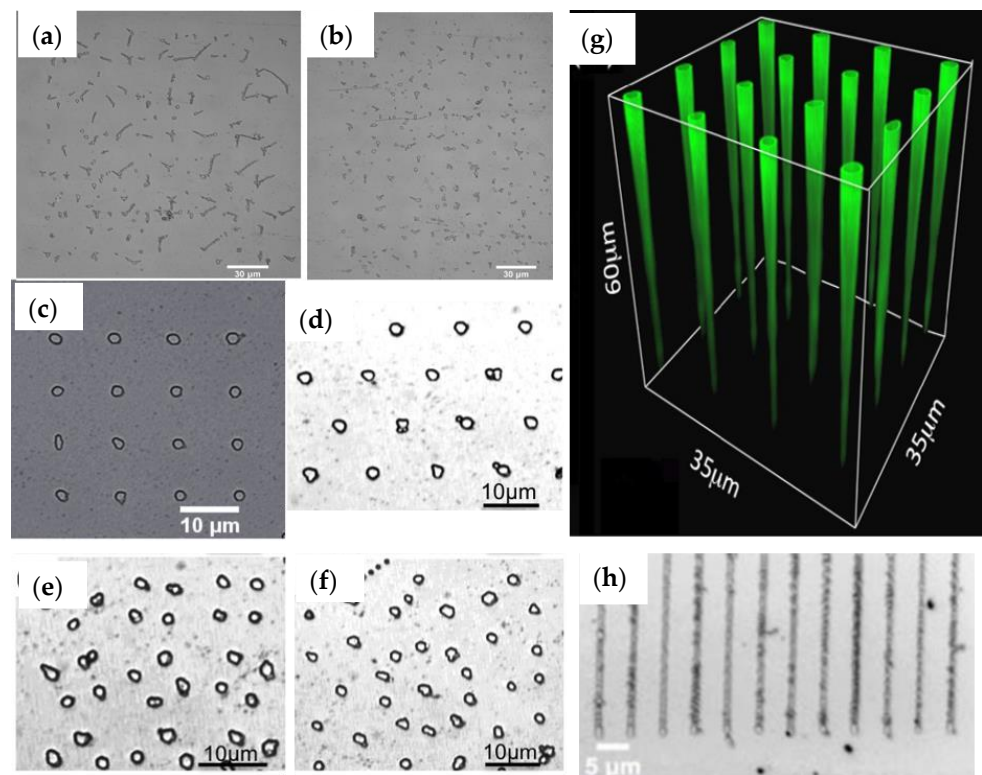


**Figure 3.** Ferroelectric domain patterns fabricated with near-infrared femtosecond laser pulses. (a) and (b) were written at 700 mW using numerical apertures 0.2 and 0.3, respectively. All other patterns in (c–h) were written at 300 mW using NA 0.65. (a–f,h) are optical microscopic images of domain patterns after chemical etching. (g) 3D image of domain pattern obtained with Cherenkov second harmonic microscopy.

The infrared-induced inverted domains extend from −Z to over 60  $\mu\text{m}$  inside the crystal, as indicated by the Cherenkov second harmonic microscopy images in Figure 3g. This is a great advantage over the UV poling, in which domain inversions were restricted to rather shallow layers close to the surface. The illuminations by near-infrared laser pulses led to ferroelectric domain inversion without destroying the crystal structure. Therefore, this

method allows the highest modulation depth of nonlinearity from  $+\chi^{(2)}$  to  $-\chi^{(2)}$  without introducing additional scattering or reflection loss for the interacting waves. For instance, a second harmonic conversion efficiency of 17.45% was achieved in a 10 mm long domain structure optically inscribed in a LiNbO<sub>3</sub> waveguide [38].

Figure 4 summarizes various domain structures fabricated in LiNbO<sub>3</sub> for applications in nonlinear wave interactions. Figure 4a shows a sunflower domain pattern, composed of more than 3000 inverted domains with an average radius of 1  $\mu\text{m}$ , for broadband Cherenkov second harmonic generation [39]. Figure 4b,c display straight and curved fork-shaped domain gratings for normal and perfect second harmonic vortex beam generation [41]. Figure 4d shows a detour holographic domain structure for H-shaped second harmonic generation (Figure 4e) from a fundamental Gaussian beam [43]. In addition, the ferroelectric domain structures created with the infrared laser pulses were used to verify the self-healing property of a nonlinear Talbot effect [77].

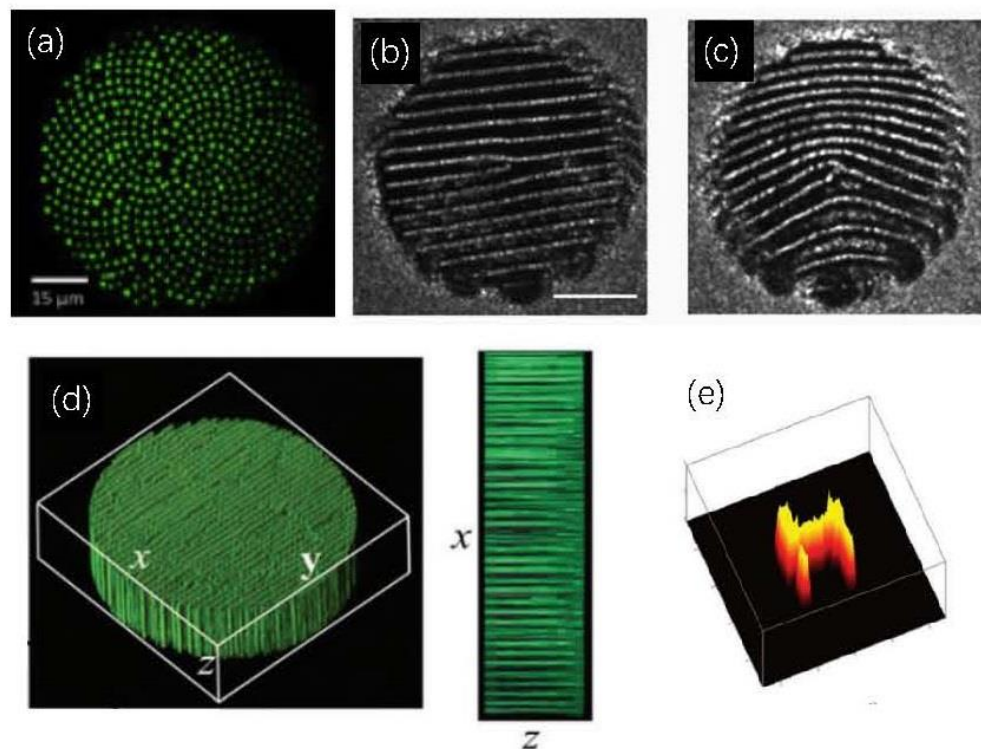


**Figure 4.** Optically induced ferroelectric domain patterns in a monodomain LiNbO<sub>3</sub> crystal. (a) A sunflower pattern created for broadband Cherenkov second harmonic generation [39]. Scale bar: 15  $\mu\text{m}$ . (b,c) Straight and curved fork-shaped domain gratings for normal and perfect vortex second harmonic generation [41]. (d) The fabricated nonlinear detour holographic structure and (e) H-shaped second harmonic observed in this structure [43].

It has been recently demonstrated that ferroelectric domain inversion in an LiNbO<sub>3</sub> crystal can also be realized with a femtosecond laser operating at 1035 nm [78] rather than the previously used 800 nm. In this case, a fiber laser (Huaray HR-Femto 10) with a pulse width of 350 fs and a repetition frequency of 1 MHz was used. Similarly to the case of domain inversion with laser pulses at 800 nm, the laser beam was first focused on the  $-Z$  surface of the crystal, then moved toward the  $Z$  surface at an average speed of 50  $\mu\text{m/s}$ . The weak focusing resulted only in randomly distributed inverted domains; regularly inverted domains appear only under conditions of sufficiently high laser power densities.

In closing this section, it is worth mentioning a recent work on laser-induced two- and three-dimensional nanodomain structures in lithium niobate [46]. In that work, a femtosecond infrared laser beam was tightly focused inside a lithium niobate sample and subsequently spatially scanned. The nonlinear absorption of light caused local heating

of the crystal and the appearance of a thermal-electric field, resulting in the formation of ferroelectric nanodomain patterns. Domains as thin as tens of nanometers were fabricated. By varying the writing direction, a previously written domain could be erased, enabling the fabrication of fully three-dimensional discrete nanodomain structures.

### 6. Femtosecond-Light-Induced Domain Inversion in MgO-Doped LiNbO<sub>3</sub> Crystals

MgO-doped LiNbO<sub>3</sub> crystal has a higher optical damage threshold than the congruent one, and hence is extremely useful in applications requiring intense light interactions. The femtosecond laser writing technique has been recently used to produce local domain inversions in MgO-doped LiNbO<sub>3</sub> crystals [79]. The process usually involves two kinds of material changes by femtosecond laser pulses, namely the permanent defects/tracks or modified crystal structures directly created in the focal volume of femtosecond laser pulses, and the accompanying inverted domains beneath/above the laser-induced permanent changes, as shown in Figure 5a [80]. This kind of inverted domain can be stimulated to grow up to 800 μm by post-thermal treatment (Figure 5b–g) [81] or illumination using femtosecond laser pulses [82].

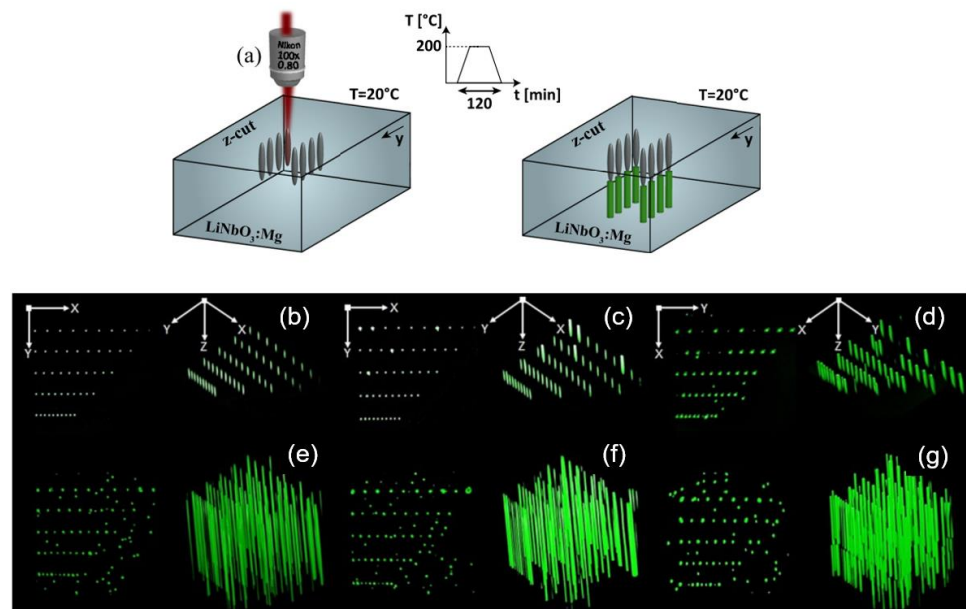


**Figure 5.** (a) Schematic illustration of two-step ferroelectric domain engineering with femtosecond laser pulses [80]. First, the focused laser beam is used to produce permanent filaments (gray) in the crystal. The sample is heated up and then cooled down to create inverted domains (green) below the permanent changes. (b–d) Cherenkov second harmonic microscopic images of the filaments after laser irradiation of different pulse energies and (e–g) the corresponding ferroelectric domains after temperature treatment [81].

It is also found that the post illumination of femtosecond laser pulses can not only stimulate further growth of previously existing inverted domains (writing operation), but also erase them (erasing operation). As shown in Figure 6, the inverted domains in a z-cut 5% MgO-doped LiNbO<sub>3</sub> crystal can be either cleared completely in the erasing operation or elongated simultaneously in the writing operation, depending on the laser focusing depth. Additionally, after being cleared completely, the original domain structures can be written again by a single writing operation. This capacity greatly improves the efficiency and flexibility of engineering ferroelectric domain structures with femtosecond laser pulses.

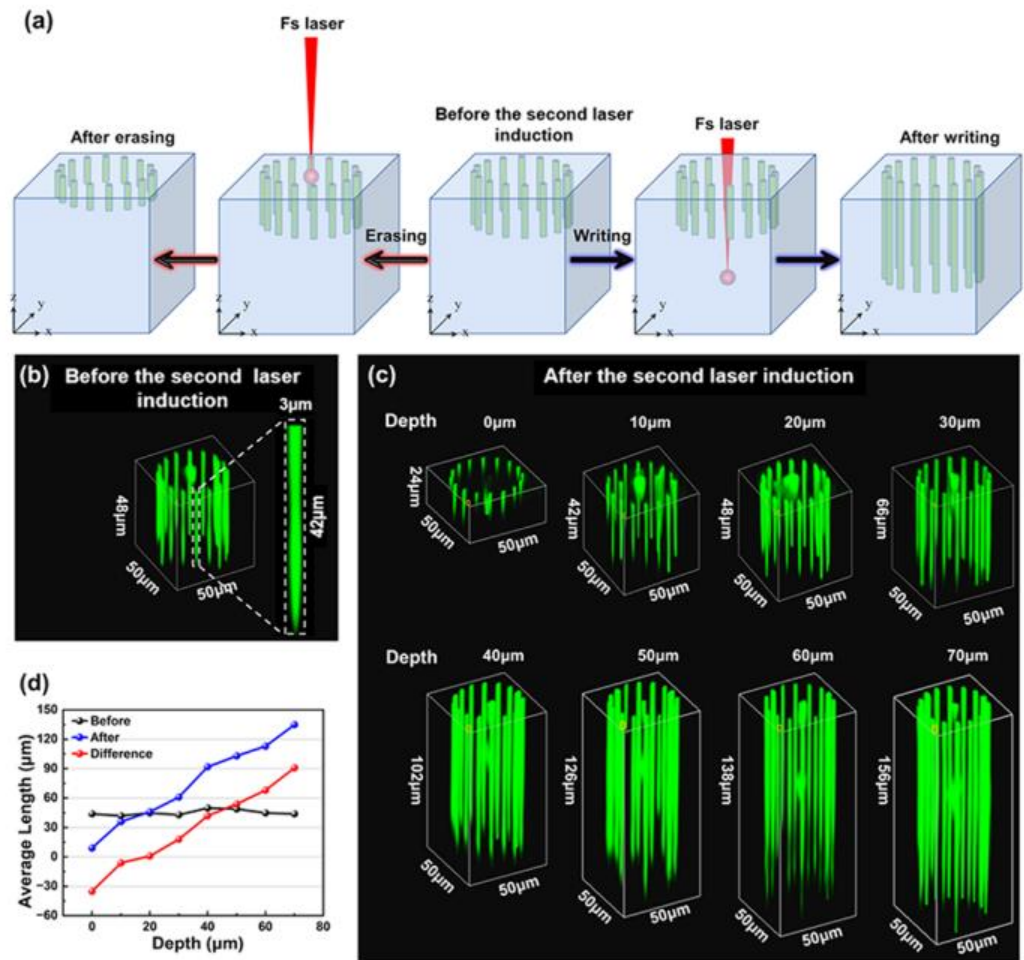


**Figure 6.** (a) Illustrating the domain erasing operation or writing operation with femtosecond laser pulses, depending on the laser focusing depth. (b) The previously existing domains before laser illuminations. (c) The post laser illuminations lead to the shortening of inverted domains when the focusing depth is less than 20 μm, but cause elongation when focused at deeper positions. (d) The average length of domains before and after the post laser induction with different laser focusing depths [83].

### 7. Three-Dimensional Domain Formation in Barium Calcium Titanate ( $Ba_xCa_{1-x}TiO_3$ , BCT), Calcium Barium Niobate ( $Ca_xBa_{1-x}Nb_2O_6$ , CBN) and Strontium Barium Niobate ( $Sr_xBa_{1-x}Nb_2O_6$ , SBN) Crystals with Femtosecond Light

Compared with  $LiNbO_3$ , BCT, CBN, and SBN crystals have lower coercive fields and hence are commonly used in 3D domain engineering. These crystals are usually multi-domain. As mentioned above, the as-grown CBN and SBN crystals have antiparallel  $180^\circ$  domains along the  $c$ -axis of the crystal. These domains are needle-shaped, with a length ranging from hundreds of nanometers to several micrometers (Figure 7a,b). In BCT, antiparallel  $180^\circ$  domains exist in all three crystallographic  $a$ ,  $b$ , and  $c$  axes. Therefore,  $90^\circ$  domain walls are formed along  $[110]$  and the equivalent directions (Figure 7c). Note that all the laser poling experiments in multi-domain crystals were conducted in  $180^\circ$  domain areas.

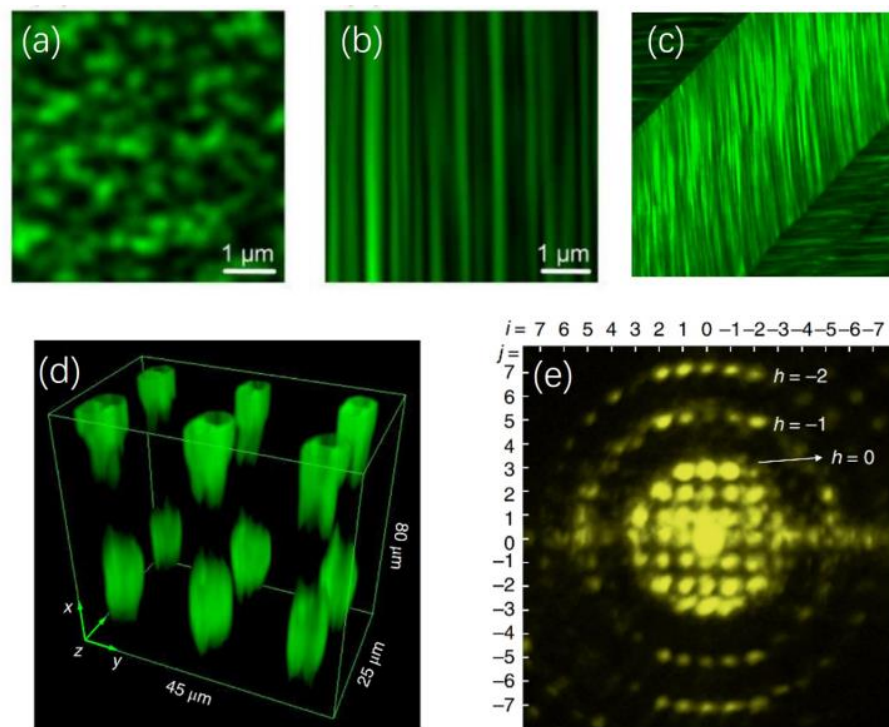


**Figure 7.** (a,b) The naturally random ferroelectric domain structures in an as-grown SBN crystal in the  $xy$  and  $xz$  planes, respectively. (c) The ferroelectric domains in a BCT crystal, where differently oriented  $180^\circ$  domains form  $90^\circ$  domain walls. (d) Femtosecond laser-induced 3D ferroelectric domain structure in a BCT crystal, imaged using Cherenkov second harmonic microscopy. The background domains are not shown in this graph because the Cherenkov second harmonic signals generated by the light-induced domains are much stronger than those from the background domains. (e) The second harmonic generation in optically induced ferroelectric domains shown in (d). The bright spots scattered on homocentric rings correspond to phase matching with different longitudinal reciprocal lattice vectors (indexed by  $h$  in the graph) [36].

The first artificially ordered 3D domain structure was experimentally demonstrated in an  $x$ -cut BCT crystal. By focusing femtosecond laser pulses at 800 nm into  $180^\circ$  random domain areas, nano-sized domains were locally realigned and merged into a  $\theta$ -shaped domain consisting of two large single domains with opposite directions of spontaneous polarization. By scanning the focus of the laser beam along three dimensions inside the crystal, a 3D domain structure was created (Figure 7d). The realization of a 3D domain's structure is one of the most important advantages of femtosecond laser poling. The 3D domain patterns were subsequently used to control the emission angles of Cherenkov second harmonic generations in BCT crystal (Figure 7e) [36]. It is worth noting that the  $90^\circ$  domain walls in BCT are detrimental to applications due to unavoidable scattering and reflection losses.

Compared with BCT crystals, there are only  $180^\circ$  domains in as-grown CBN and SBN crystals. The laser poling in these two crystals was realized with Ti: a sapphire femtosecond laser source operating at 800 nm. Figure 8 depicts typical domain structures created in these crystals, including the nonlinear volume holographic structure for more efficient second harmonic vortex beam generation (Figure 8a,b) [42], multi-layer domain patterns for dynamic nonlinear wave front shaping (Figure 8c,d) [40], a four-grating structure for collinear generation of a second harmonic vortex beam (Figure 8e,f) [84], and a holographic domain pattern for second harmonic bottle beam generation (Figure 8g,h) [85].

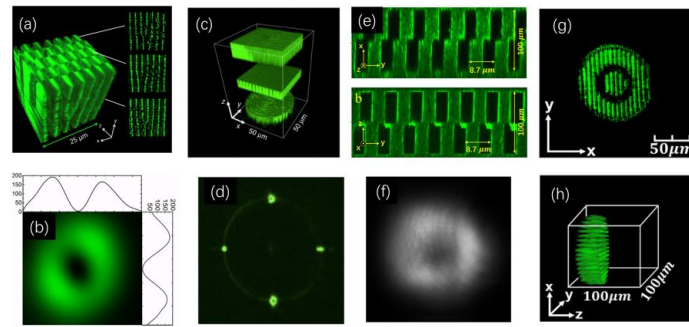


**Figure 8.** The various ferroelectric domain structures fabricated in CBN and SBN crystals using femtosecond laser poling. (a) An example of nonlinear volume holograms formed in a CBN crystal and (b) the observed second harmonic vortex beam generation in this structure [42]. (c) The multi-layer domain structure and (d) the generated second harmonic with various wavefronts in a CBN crystal [40]. (e) The four-grating domain structure for (f) collinear generation of second harmonic vortex beam in CBN crystal [84]. (g,h) The ferroelectric domain patterns fabricated in an SBN crystal for second harmonic bottle-shaped beam generation [85].

For an SBN crystal, the influences of laser parameters and poling conditions were systematically studied in the experiment described in [86]. It was shown that the femtosecond laser poling of a ferroelectric crystal is not a narrow-band effect, which means domain inversion can occur at a relatively broad spectral range if the nonlinear absorption of photons by the material can take place. There is an optimal spectral range at which the threshold power for domain inversion is the lowest, according to the strongest two-photon absorption wavelength of an SBN crystal (see Figure 9a,b). It was also demonstrated that stronger laser pulses and longer exposure times are beneficial to creations of longer and bigger inverted domains (Figure 9c,d). Meanwhile, pushing the laser focus toward the rear surface for a certain distance also contributes to longer inverted domains in SBN crystals (Figure 9e).

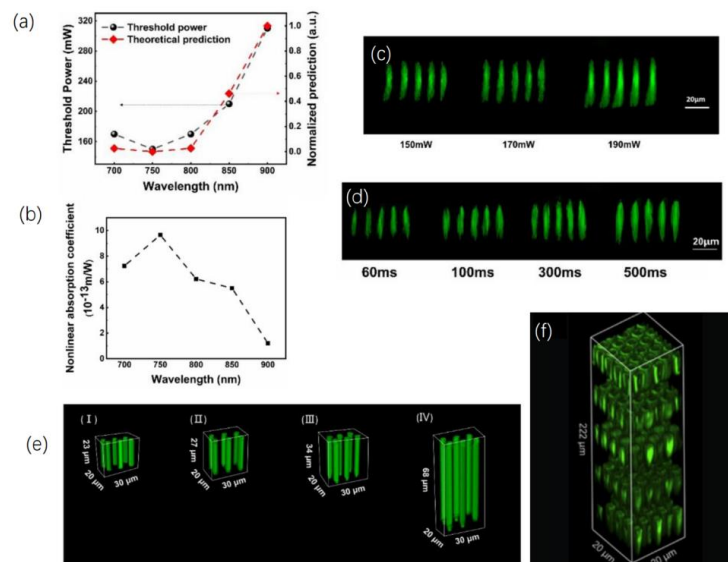


**Figure 9.** The influences of laser poling parameters and conditions on ferroelectric domain inversion in an SBN crystal [86]. (a) The variation of threshold laser power for optically induced domain inversion with different wavelengths of writing beam. (b) The measured nonlinear absorption coefficient at the corresponding wavelengths. (c,d) The Cherenkov second harmonic microscopic images of ferroelectric domain structures fabricated using different laser powers and exposure time, respectively. (e) The variation of the length of inverted domains with the moving distance of the focus of the writing laser beam (I, 1  $\mu\text{m}$ ; II, 5  $\mu\text{m}$ ; III, 10  $\mu\text{m}$ ; IV, 370  $\mu\text{m}$ ). All the figures above are published with permission [86]. (f) The 3D ferroelectric domain structures fabricated in a single-domain CBN crystal [61].

To eliminate the influence of random antiparallel domains, a multi-domain CBN crystal was first converted into a single-domain crystal using the electric field poling method [61]. This was done by applying an electric field of 400 V/mm along the Z axis of the crystal, which was kept at 200 °C for half an hour and subsequently slowly cooled to room temperature. Then the femtosecond laser writing of 3D domain structures was conducted in the single-domain CBN crystal. The created domain structures are shown in Figure 9f.

### 8. Femtosecond Laser Poling of $0.62\text{Pb}(\text{Mg}_{1/3}\text{Nb}_{2/3})\text{O}_3\text{-}0.38\text{PbTiO}_3$ (PMN-38PT) Crystal

$\text{LiNbO}_3$ , BCT, SBN, and CBN crystals are well known for their excellent nonlinear optical and electro-optical properties. Compared with them, PMN-PT crystals received great interest because of their huge piezo-electric response [87]. Among them, the specific component PMN-38PT crystal exhibits a tetragonal phase and can also be relatively easily induced to present a single-domain state, which is crucial for practical domain-based devices. In 2022, the optical poling of PMN-PT crystal was realized with a femtosecond laser operating at 800 nm [62]. There are two types of inverted domains optically formed in the PMN-38PT crystal, depending on the power of the writing laser pulses. Primary domains are formed in the focal volume of the beam. Secondary domains appear at higher laser power, in the shape of hollow cylindrical structures surrounding the beam (Figure 10a). The appearance of the primary domains is governed by the same physical mechanism as those in SBN, CBN, and  $\text{LiNbO}_3$  crystals. However, the secondary type of hollow cylindrical domains has so far only been observed in PMN-38PT crystals. It is believed the optically induced thermoelectric and space charge fields play key roles in their formations [62].

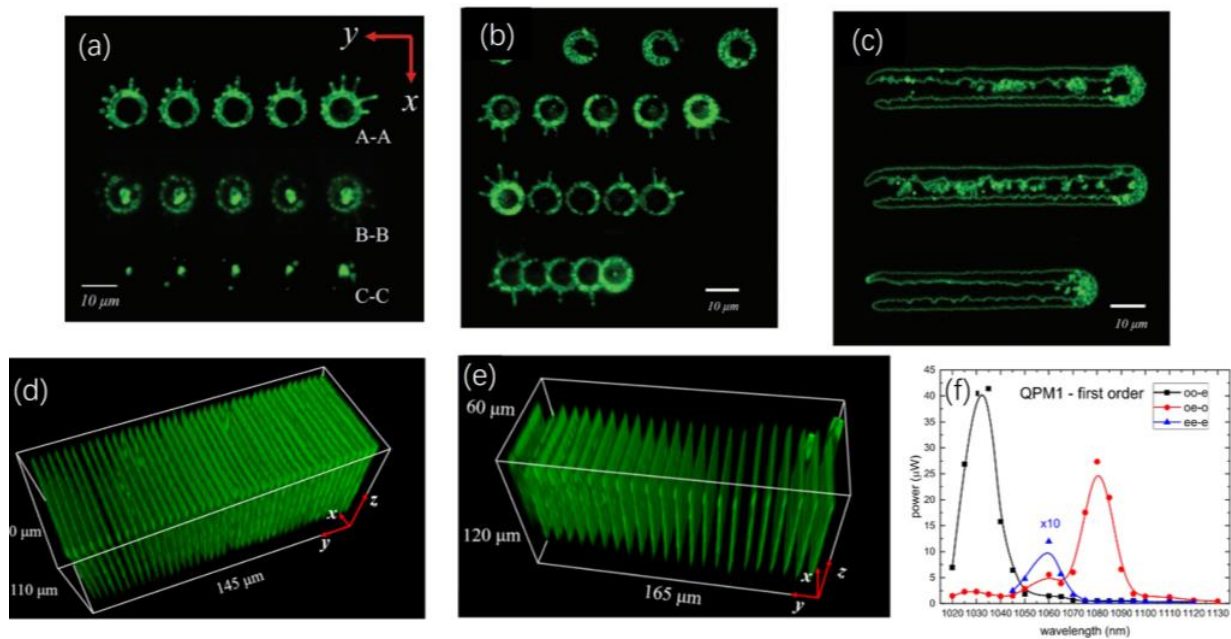


**Figure 10.** (a) The primary and secondary kinds of ferroelectric domain structure written by femtosecond laser pulses in a PMN-38PT crystal [62]. (b,c) Cherenkov second harmonic microscopic images of the secondary type of inverted domains formed with different separation distances [62]. (d,e) Two periodic ferroelectric domain structures created in a PMN-38PT crystal for quasi-phase matching second harmonic generation and the measured second harmonic resonant wavelengths [88]. (f) Second harmonic signal generated in the structure from (d) as a function of the wavelength of the input fundamental beam. Three different types of interaction involving different polarization components of the input beams are shown.

Another important effect observed in PMN-38PT crystals is the erasure of the originally formed domains by newly formed domains if they overlap. Figure 10b depicts a few periodic sequences of secondary domains fabricated with different separations. In each sequence, the domains were written from left to right. With domain separations smaller than the diameter of the secondary domain, the newly formed domain erases the right part of the preceding domain. This effect becomes even more pronounced at separations of less than 2  $\mu\text{m}$ . Every time a new domain is formed, it completely erases the right half of the preceding domain. Repeating the process leads to the formation of the long U-shaped secondary domain, as seen in Figure 10c.

The high quality of light-induced domain structures in PMN-38PT crystals was confirmed by quasi-phase matched second harmonic generation in these structures [88]. Two typical structures with different periods and lengths were fabricated using femtosecond laser poling. They are depicted in Figures 10d and 10e, respectively. The first one is 2 mm long with a period of 3.5  $\mu\text{m}$ , and the second is 1.13 mm long with a period of 7.1  $\mu\text{m}$ . In both structures, the quasi-phase matched second harmonic generation was observed, with different types of interactions involving various polarization and nonlinear coefficients (Figure 10f).

## 9. Conclusions

We have reviewed recent research progresses on femtosecond laser poling of ferroelectric crystals. Various ferroelectric domain structures, including 2D and 3D periodic lattices, fork-shaped gratings, and nonlinear holographic structures formed in  $\text{LiNbO}_3$ , BCT, SBN, CBN, and PMN-38PT crystals have been summarized. The influences of laser writing conditions and parameters on the morphologies of light-induced inverted domains have been also discussed, with the SBN crystal being investigated as a representative. In addition to the femtosecond laser poling technique itself, the resulting applications of these laser-fabricated domain structures in nonlinear optics are also mentioned, focusing mainly on laser frequency and nonlinear wavefront shaping.

Compared with intensive studies that have been devoted to the fabrication and application of light-induced ferroelectric domains, the exploration of the physical mechanism of femtosecond laser poling is still at an early stage. The thermoelectric field model is effective to explain most of the experimental results, but there are still subtle effects that are waiting for further explanations. For example, it has been found that light-induced domain inversion can be stimulated by post-heating or post-exposure. However, the physical reasons and factors affecting this effect are still not fully understood. In future work, the influence of laser beam conditions such as wavelength and optical power on the morphologies of inverted domains needs to be systematically examined using a wide variety of ferroelectric crystals. Furthermore, the role of laser repetition rate, pulse duration, and crystal temperatures should be investigated, as they are critical factors affecting the thermoelectric field in the current poling model.

Another major challenge is to optimize the laser poling technique in order to write deeper and more quickly into the nonlinear crystal to support the fabrication of large-scale ferroelectric domain structures for nonlinear and quantum optical applications. Finally, the nonlinear optical interactions in femtosecond laser induced ferroelectric domains need to be realized with higher efficiencies. An important aspect in this context is to further reduce the modification of the linear index by the laser writing process. These small modifications lead to reflections and the scattering of light, which limits the efficient interaction length in the nonlinear photonic crystal. Were the abovementioned challenges to be overcome, the femtosecond laser poling of ferroelectric crystals would find more applications in applied optics, quantum optics, and electronic technologies.

**Author Contributions:** Writing—original draft preparation, X.C. and Y.S.; writing—review and editing, Y.S., S.L., T.X., R.Z. and W.K.; supervision, Y.S. and W.K.; project administration, Y.S. and W.K.; funding acquisition, Y.S. and W.K. All authors have read and agreed to the published version of the manuscript.

**Funding:** This work was funded by the National Natural Science Foundation of China (Nos. 12274248, 62275136, and 12361141815), Natural Science Foundation of Shaanxi Province (2023-JC-QN-0014), Natural Science Foundation of Guangdong Province (2023A1515012928), Australian Research Council, and the K. C. Wong Magna Fund of Ningbo University.

**Acknowledgments:** We acknowledge Yunze Wang and Xiaokang Hu for their help in the preparation of the figures used in this manuscript.

**Conflicts of Interest:** The authors declare no conflicts of interest.

## References

1. Gattass, R.R.; Mazur, E. Femtosecond laser micromachining in transparent materials. *Nat. Photonics* **2008**, *2*, 219–225. [[CrossRef](#)]
2. Marcinkevičius, A.; Juodkazis, S.; Watanabe, M.; Miwa, M.; Matsuo, S.; Misawa, H.; Nishii, J. Femtosecond laser-assisted three-dimensional microfabrication in silica. *Opt. Lett.* **2001**, *26*, 277–279. [[CrossRef](#)] [[PubMed](#)]
3. Ku, J.-F.; Chen, Q.-D.; Zhang, R.; Sun, H.-B. Whispering-gallery-mode microdisk lasers produced by femtosecond laser direct writing. *Opt. Lett.* **2011**, *36*, 2871–2873. [[CrossRef](#)] [[PubMed](#)]
4. Srisungsitthisunti, P.; Ersoy, O.K.; Xu, X. Volume Fresnel zone plates fabricated by femtosecond laser direct writing. *Appl. Phys. Lett.* **2007**, *90*, 011104. [[CrossRef](#)]
5. Maruo, S.; Saeki, T. Femtosecond laser direct writing of metallic microstructures by photoreduction of silver nitrate in a polymer matrix. *Opt. Express* **2008**, *16*, 1174–1179. [[CrossRef](#)] [[PubMed](#)]
6. Yong, J.; Huo, J.; Yang, Q.; Chen, F.; Fang, Y.; Wu, X.; Liu, L.; Lu, X.; Zhang, J.; Hou, X. Femtosecond Laser Direct Writing of Porous Network Microstructures for Fabricating Super-Slippery Surfaces with Excellent Liquid Repellence and Anti-Cell Proliferation. *Adv. Mater. Interfaces* **2018**, *5*, 1701479. [[CrossRef](#)]
7. Hanada, Y.; Sugioka, K.; Kawano, H.; Ishikawa, I.S.; Miyawaki, A.; Midorikawa, K. Nano-aquarium for dynamic observation of living cells fabricated by femtosecond laser direct writing of photostructurable glass. *Biomed. Microdevices* **2008**, *10*, 403–410. [[CrossRef](#)]
8. Xu, B.-B.; Zhang, Y.-L.; Xia, H.; Dong, W.-F.; Ding, H.; Sun, H.-B. Fabrication and multifunction integration of microfluidic chips by femtosecond laser direct writing. *Lab Chip* **2013**, *13*, 1677–1690. [[CrossRef](#)] [[PubMed](#)]
9. Sun, Y.-L.; Dong, W.-F.; Niu, L.-G.; Jiang, T.; Liu, D.-X.; Zhang, L.; Wang, Y.-S.; Chen, Q.-D.; Kim, D.-P.; Sun, H.-B. Protein-based soft micro-optics fabricated by femtosecond laser direct writing. *Light-Sci. Appl.* **2014**, *3*, e129. [[CrossRef](#)]
10. Consales, M.; Ricciardi, A.; Crescitelli, A.; Esposito, E.; Cutolo, A.; Cusano, A. Lab-on-fiber technology: Toward multifunctional optical nanoprobes. *ACS Nano* **2012**, *6*, 3163–3170. [[CrossRef](#)]
11. Pisco, M.; Galeotti, F.; Quero, G.; Grisci, G.; Micco, A.; Mercaldo, L.V.; Veneri, P.D.; Cutolo, A.; Cusano, A. Nanosphere lithography for optical fiber tip nanoprobes. *Light-Sci. Appl.* **2017**, *6*, e16229. [[CrossRef](#)] [[PubMed](#)]
12. Ho, S.; Herman, P.R.; Aitchison, J.S. Single-and multi-scan femtosecond laser writing for selective chemical etching of cross section patternable glass micro-channels. *Appl. Phys. A* **2012**, *106*, 5–13. [[CrossRef](#)]
13. Haque, M. Chemical-Assisted Femtosecond Laser Writing of Lab-in-Fiber Sensors. Ph.D. Thesis, University of Toronto, Toronto, ON, Canada, 2014.
14. Fahy, S.; Merlin, R. Reversal of ferroelectric domains by ultrashort optical pulses. *Phys. Rev. Lett.* **1994**, *73*, 1122. [[CrossRef](#)] [[PubMed](#)]
15. Berger, V. Nonlinear Photonic Crystals. *Phys. Rev. Lett.* **1998**, *81*, 4136–4139. [[CrossRef](#)]
16. Armstrong, J.A.; Bloembergen, N.; Ducuing, J.; Pershan, P.S. Interactions between Light Waves in a Nonlinear Dielectric. *Phys. Rev.* **1962**, *127*, 1918–1939. [[CrossRef](#)]
17. Zhu, S.; Zhu, Y.; Ming, N.b. Quasi-Phase-Matched Third-Harmonic Generation in a Quasi-Periodic Optical Superlattice. *Science* **1997**, *278*, 843–846. [[CrossRef](#)]
18. Ellenbogen, T.; Voloch-Bloch, N.; Ganany-Padowicz, A.; Arie, A. Nonlinear generation and manipulation of Airy beams. *Nat. Photonics* **2009**, *3*, 395–398. [[CrossRef](#)]
19. Matsumo, S.; Lim, E.J.; Hertz, H.M.; Fejer, M.M. Quasiphase-matched second harmonic generation of blue light lithium tantalate waveguides in electrically periodically-poled. *Electron. Lett.* **1991**, *27*, 2040–2041. [[CrossRef](#)]
20. Arimoto, Y.; Ishiwara, H. Current status of ferroelectric random-access memory. *Mrs Bull.* **2004**, *29*, 823–828. [[CrossRef](#)]
21. Zhang, Y.; Sheng, Y.; Zhu, S.; Xiao, M.; Krolikowski, W. Nonlinear photonic crystals: From 2D to 3D. *Optica* **2021**, *8*, 372–381. [[CrossRef](#)]
22. Agronin, A.; Rosenwaks, Y.; Rosenman, G. Ferroelectric domain reversal in LiNbO<sub>3</sub> crystals using high-voltage atomic force microscopy. *Appl. Phys. Lett.* **2004**, *85*, 452–454. [[CrossRef](#)]

23. Restoin, C.; Darraud-Taupiac, C.; Decossas, J.L.; Vareille, J.C.; Hauden, J.; Martinez, A. Ferroelectric domain inversion by electron beam on LiNbO<sub>3</sub> and Ti:LiNbO<sub>3</sub>. *J. Appl. Phys.* **2000**, *88*, 6665–6668. [[CrossRef](#)]
24. Fujimura, A.; Sohmura, T.; Suhara, T. Fabrication of domain-inverted gratings in MgO:LiNbO<sub>3</sub> by applying voltage under ultraviolet irradiation through photomask at room temperature. *Electron. Lett.* **2003**, *39*, 719–721. [[CrossRef](#)]
25. Manz, S.; Matsubara, M.; Lottermoser, T.; Büchi, J.; Iyama, A.; Kimura, T.; Meier, D.; Fiebig, M. Reversible optical switching of antiferromagnetism in TbMnO<sub>3</sub>. *Nat. Photonics* **2016**, *10*, 653–656. [[CrossRef](#)]
26. Iurchuk, V.; Schick, D.; Bran, J.; Colson, D.; Forget, A.; Halley, D.; Koc, A.; Reinhardt, M.; Kwamen, C.; Morley, N.A.; et al. Optical Writing of Magnetic Properties by Remanent Photostriction. *Phys. Rev. Lett.* **2016**, *117*, 107403. [[CrossRef](#)] [[PubMed](#)]
27. Sando, D.; Yang, Y.R.; Bousquet, E.; Carrétéro, C.; Garcia, V.; Fusil, S.; Dolfi, D.; Barthélémy, A.; Ghosez, P.; Bellaiche, L.; et al. Large elasto-optic effect and reversible electrochromism in multiferroic BiFeO<sub>3</sub>. *Nat. Commun.* **2016**, *7*, 10718. [[CrossRef](#)] [[PubMed](#)]
28. Wengler, M.C.; Heinemeyer, U.; Soergel, E.; Buse, K. Ultraviolet light-assisted domain inversion in magnesium-doped lithium niobate crystals. *J. Appl. Phys.* **2005**, *98*, 064104. [[CrossRef](#)]
29. Mailis, S.; Riziotis, C.; Smith, P.G.R.; Scott, J.G.; Eason, R.W. Continuous wave ultraviolet radiation induced frustration of etching in lithium niobate single crystals. *Appl. Surf. Sci.* **2003**, *206*, 46–52. [[CrossRef](#)]
30. Muir, A.C.; Sones, C.L.; Mailis, S.; Eason, R.W.; Jungk, T.; Hoffmann, A.; Soergel, E. Direct-writing of inverted domains in lithium niobate using a continuous wave ultra violet laser. *Opt. Express* **2008**, *16*, 2336–2350. [[CrossRef](#)] [[PubMed](#)]
31. Steigerwald, H.; Ying, Y.J.; Eason, R.W.; Buse, K.; Mailis, S.; Soergel, E. Direct writing of ferroelectric domains on the x- and y-faces of lithium niobate using a continuous wave ultraviolet laser. *Appl. Phys. Lett.* **2011**, *98*, 062902. [[CrossRef](#)]
32. Mailis, S.; Brown, P.T.; Sones, C.L.; Zergioti, I.; Eason, R.W. Etch frustration in congruent lithium niobate single crystals induced by femtosecond ultraviolet laser irradiation. *Appl. Phys. A-Mater.* **2002**, *74*, 135–137. [[CrossRef](#)]
33. Valdivia, C.E.; Sones, C.L.; Scott, J.G.; Mailis, S.; Eason, R.W.; Scrymgeour, D.A.; Gopalan, V.; Jungk, T.; Soergel, E.; Clark, I. Nanoscale surface domain formation on the z face of lithium niobate by pulsed ultraviolet laser illumination. *Appl. Phys. Lett.* **2005**, *86*, 022906. [[CrossRef](#)]
34. Kuznetsov, D.K.; Shur, V.Y.; Negashev, S.A.; Lobov, A.I.; Pelegov, D.V.; Shishkin, E.I.; Zelenovskiy, P.S.; Platonov, V.V.; Ivanov, M.G.; Osipov, V.V. Formation of Nano-Scale Domain Structures in Lithium Niobate Using High-Intensity Laser Irradiation. *Ferroelectrics* **2008**, *373*, 133–138. [[CrossRef](#)]
35. Shur, V.Y.; Kuznetsov, D.K.; Mingaliev, E.A.; Yakunina, E.M.; Lobov, A.I.; Ievlev, A.V. In situ investigation of formation of self-assembled nanodomain structure in lithium niobate after pulse laser irradiation. *Appl. Phys. Lett.* **2011**, *99*, 082901. [[CrossRef](#)]
36. Xu, T.; Switkowski, K.; Chen, X.; Liu, S.; Koynov, K.; Yu, H.; Zhang, H.; Wang, J.; Sheng, Y.; Krolikowski, W. Three-dimensional nonlinear photonic crystal in ferroelectric barium calcium titanate. *Nat. Photonics* **2018**, *12*, 591–595. [[CrossRef](#)]
37. Chen, X.; Karpinski, P.; Shvedov, V.; Koynov, K.; Wang, B.; Trull, J.; Cojocar, C.; Krolikowski, W.; Sheng, Y. Ferroelectric domain engineering by focused infrared femtosecond pulses. *Appl. Phys. Lett.* **2015**, *107*, 141102. [[CrossRef](#)]
38. Chen, X.; Karpinski, P.; Shvedov, V.; Boes, A.; Mitchell, A.; Krolikowski, W.; Sheng, Y. Quasi-phase matching via femtosecond laser-induced domain inversion in lithium niobate waveguides. *Opt. Lett.* **2016**, *41*, 2410–2413. [[CrossRef](#)] [[PubMed](#)]
39. Liu, S.; Switkowski, K.; Chen, X.; Xu, T.; Krolikowski, W.; Sheng, Y. Broadband enhancement of Cerenkov second harmonic generation in a sunflower spiral nonlinear photonic crystal. *Opt. Express* **2018**, *26*, 8628–8633. [[CrossRef](#)]
40. Liu, S.; Switkowski, K.; Xu, C.; Tian, J.; Wang, B.; Lu, P.; Krolikowski, W.; Sheng, Y. Nonlinear wavefront shaping with optically induced three-dimensional nonlinear photonic crystals. *Nat. Commun.* **2019**, *10*, 3208. [[CrossRef](#)] [[PubMed](#)]
41. Liu, D.; Liu, S.; Mazur, L.M.; Wang, B.; Lu, P.; Krolikowski, W.; Sheng, Y. Smart optically induced nonlinear photonic crystals for frequency conversion and control. *Appl. Phys. Lett.* **2020**, *116*, 051104. [[CrossRef](#)]
42. Liu, S.; Mazur, L.M.; Krolikowski, W.; Sheng, Y. Nonlinear Volume Holography in 3D Nonlinear Photonic Crystals. *Laser Photonics Rev.* **2020**, *14*, 2000224. [[CrossRef](#)]
43. Wang, B.; Hong, X.; Wang, K.; Chen, X.; Liu, S.; Krolikowski, W.; Lu, P.; Sheng, Y. Nonlinear detour phase holography. *Nanoscale* **2021**, *13*, 2693–2702. [[CrossRef](#)] [[PubMed](#)]
44. Ying, C.Y.J.; Muir, A.C.; Valdivia, C.E.; Steigerwald, H.; Sones, C.L.; Eason, R.W.; Soergel, E.; Mailis, S. Light-mediated ferroelectric domain engineering and micro-structuring of lithium niobate crystals. *Laser Photonics Rev.* **2012**, *6*, 526–548. [[CrossRef](#)]
45. Wei, D.; Wang, C.; Wang, H.; Hu, X.; Wei, D.; Fang, X.; Zhang, Y.; Wu, D.; Hu, Y.; Li, J.; et al. Experimental demonstration of a three-dimensional lithium niobate nonlinear photonic crystal. *Nat. Photonics* **2018**, *12*, 596–600. [[CrossRef](#)]
46. Xu, X.; Wang, T.; Chen, P.; Zhou, C.; Ma, J.; Wei, D.; Wang, H.; Niu, B.; Fang, X.; Wu, D.; et al. Femtosecond laser writing of lithium niobate ferroelectric nanodomains. *Nature* **2022**, *609*, 496–501. [[CrossRef](#)] [[PubMed](#)]
47. Lu, Y.-Q.; Zhu, Y.-Y.; Chen, Y.-F.; Zhu, S.-N.; Ming, N.-B.; Feng, Y.-J. Optical properties of an ionic-type phononic crystal. *Science* **1999**, *284*, 1822–1824. [[CrossRef](#)] [[PubMed](#)]
48. Yudistira, D.; Benchabane, S.; Janner, D.; Pruner, V. Surface acoustic wave generation in ZX-cut LiNbO<sub>3</sub> superlattices using coplanar electrodes. *Appl. Phys. Lett.* **2009**, *95*, 052901. [[CrossRef](#)]
49. Yudistira, D.; Boes, A.; Rezk, A.R.; Yeo, L.Y.; Friend, J.R.; Mitchell, A. UV direct write metal enhanced redox (MER) domain engineering for realization of surface acoustic devices on lithium niobate. *Adv. Mater. Interfaces* **2014**, *1*, 1400006. [[CrossRef](#)]
50. Chanthbouala, A.; Garcia, V.; Cherifi, R.O.; Bouzehouane, K.; Fusil, S.; Moya, X.; Xavier, S.; Yamada, H.; Deranlot, C.; Mathur, N.D. A ferroelectric memristor. *Nat. Mater.* **2012**, *11*, 860–864. [[CrossRef](#)] [[PubMed](#)]

51. Seidel, J.; Fu, D.; Yang, S.-Y.; Alarcón-Lladó, E.; Wu, J.; Ramesh, R.; Ager, J.W., III. Efficient photovoltaic current generation at ferroelectric domain walls. *Phys. Rev. Lett.* **2011**, *107*, 126805. [[CrossRef](#)] [[PubMed](#)]
52. Aird, A.; Salje, E.K. Sheet superconductivity in twin walls: Experimental evidence of WO<sub>3-x</sub>. *J. Phys-Condens. Mat.* **1998**, *10*, L377. [[CrossRef](#)]
53. Poberaj, G.; Hu, H.; Sohler, W.; Guenter, P. Lithium niobate on insulator (LNOI) for micro-photonics devices. *Laser Photonics Rev.* **2012**, *6*, 488–503. [[CrossRef](#)]
54. Chang, L.; Li, Y.; Volet, N.; Wang, L.; Peters, J.; Bowers, J.E. Thin film wavelength converters for photonic integrated circuits. *Optica* **2016**, *3*, 531–535. [[CrossRef](#)]
55. Guarino, A.; Poberaj, G.; Rezzonico, D.; Degl'Innocenti, R.; Günter, P. Electro-optically tunable microring resonators in lithium niobate. *Nat. Photonics* **2007**, *1*, 407–410. [[CrossRef](#)]
56. Boes, A.; Corcoran, B.; Chang, L.; Bowers, J.; Mitchell, A. Status and potential of lithium niobate on insulator (LNOI) for photonic integrated circuits. *Laser Photonics Rev.* **2018**, *12*, 1700256. [[CrossRef](#)]
57. Ramirez, M.; Romero, J.; Molina, P.; Bausa, L. Near infrared and visible tunability from a diode pumped Nd<sup>3+</sup> activated strontium barium niobate laser crystal. *Appl. Phys. B* **2005**, *81*, 827–830. [[CrossRef](#)]
58. Sheng, Y.; Chen, X.; Lukasiewicz, T.; Swirkowicz, M.; Koynov, K.; Krolikowski, W. Calcium barium niobate as a functional material for broadband optical frequency conversion. *Opt. Lett.* **2014**, *39*, 1330–1332. [[CrossRef](#)] [[PubMed](#)]
59. Wang, W.; Roppo, V.; Kalinowski, K.; Kong, Y.; Neshev, D.; Cojocaru, C.; Trull, J.; Vilaseca, R.; Staliunas, K.; Krolikowski, W. Third-harmonic generation via broadband cascading in disordered quadratic nonlinear media. *Opt. Express* **2009**, *17*, 20117–20123. [[CrossRef](#)]
60. Tunyagi, A.R.; Ulex, M.; Betzler, K. Noncollinear optical frequency doubling in strontium barium niobate. *Phys. Rev. Lett.* **2003**, *90*, 243901. [[CrossRef](#)]
61. Mazur, L.M.; Liu, S.; Chen, X.; Krolikowski, W.; Sheng, Y. Localized Ferroelectric Domains via Laser Poling in Monodomain Calcium Barium Niobate Crystal. *Laser Photonics Rev.* **2021**, *15*, 2100088. [[CrossRef](#)]
62. Chen, X.; Liu, D.; Liu, S.; Mazur, L.M.; Liu, X.; Wei, X.; Xu, Z.; Wang, J.; Sheng, Y.; Wei, Z.; et al. Optical Induction and Erasure of Ferroelectric Domains in Tetragonal PMN-38PT Crystals. *Adv. Opt. Mater.* **2021**, *10*, 2102115. [[CrossRef](#)]
63. Li, F.; Wang, L.; Jin, L.; Xu, Z.; Zhang, S. Achieving single domain relaxor-PT crystals by high temperature poling. *CrystEngComm* **2014**, *16*, 2892–2897. [[CrossRef](#)]
64. Sones, C.L.; Mailis, S.; Brocklesby, W.S.; Eason, R.W.; Owen, J.R. Differential etch rates in z-cut LiNbO<sub>3</sub> for variable HF/HNO<sub>3</sub> concentrations. *J. Mater. Chem.* **2002**, *12*, 295–298. [[CrossRef](#)]
65. Gruverman, A.; Alexe, M.; Meier, D. Piezoresponse force microscopy and nanoferroic phenomena. *Nat. Commun.* **2019**, *10*, 1661. [[CrossRef](#)] [[PubMed](#)]
66. Sheng, Y.; Best, A.; Butt, H.-J.; Krolikowski, W.; Arie, A.; Koynov, K. Three-dimensional ferroelectric domain visualization by Čerenkov-type second harmonic generation. *Opt. Express* **2010**, *18*, 16539–16545. [[CrossRef](#)] [[PubMed](#)]
67. Saltiel, S.M.; Sheng, Y.; Voloch-Bloch, N.; Neshev, D.N.; Krolikowski, W.; Arie, A.; Koynov, K.; Kivshar, Y.S. Čerenkov-Type Second-Harmonic Generation in Two-Dimensional Nonlinear Photonic Structures. *IEEE J. Quantum Electron.* **2009**, *45*, 1465–1472. [[CrossRef](#)]
68. Karpinski, P.; Chen, X.; Shvedov, V.; Hnatovsky, C.; Grisard, A.; Lallier, E.; Luther-Davies, B.; Krolikowski, W.; Sheng, Y. Nonlinear diffraction in orientation-patterned semiconductors. *Opt. Express* **2015**, *23*, 14903–14912. [[CrossRef](#)] [[PubMed](#)]
69. Ayoub, M.; Futterlieb, H.; Imbrock, J.; Denz, C. 3D Imaging of Ferroelectric Kinetics during Electrically Driven Switching. *Adv. Mater.* **2017**, *29*, 1603325. [[CrossRef](#)]
70. Grigoriev, A.; Do, D.-H.; Kim, D.M.; Eom, C.-B.; Adams, B.; Dufresne, E.M.; Evans, P.G. Nanosecond domain wall dynamics in ferroelectric Pb(Zr, Ti)O<sub>3</sub> thin films. *Phys. Rev. Lett.* **2006**, *96*, 187601. [[CrossRef](#)] [[PubMed](#)]
71. Zelenovskiy, P.; Fontana, M.; Shur, V.Y.; Bourson, P.; Kuznetsov, D. Raman visualization of micro-and nanoscale domain structures in lithium niobate. *Appl. Phys. A* **2010**, *99*, 741–744. [[CrossRef](#)]
72. Nelson, C.T.; Gao, P.; Jokisaari, J.R.; Heikes, C.; Adamo, C.; Melville, A.; Baek, S.-H.; Folkman, C.M.; Winchester, B.; Gu, Y. Domain dynamics during ferroelectric switching. *Science* **2011**, *334*, 968–971. [[CrossRef](#)] [[PubMed](#)]
73. Zhao, T.; Scholl, A.; Zavaliche, F.; Lee, K.; Barry, M.; Doran, A.; Cruz, M.; Chu, Y.; Ederer, C.; Spaldin, N. Electrical control of antiferromagnetic domains in multiferroic BiFeO<sub>3</sub> films at room temperature. *Nat. Mater.* **2006**, *5*, 823–829. [[CrossRef](#)] [[PubMed](#)]
74. Soergel, E. Visualization of ferroelectric domains in bulk single crystals. *Appl. Phys. B* **2005**, *81*, 729–751. [[CrossRef](#)]
75. Li, L.; Xie, L.; Pan, X. Real-time studies of ferroelectric domain switching: A review. *Rep. Prog. Phys.* **2019**, *82*, 126502. [[CrossRef](#)]
76. Luh, Y.S.; Feigelson, R.S.; Fejer, M.M.; Byer, R.L. Ferroelectric domain structures in LiNbO<sub>3</sub> single-crystal fibers. *J. Cryst. Growth* **1986**, *78*, 135–143. [[CrossRef](#)]
77. Wang, B.; Liu, S.; Xu, T.; Zhao, R.; Lu, P.; Krolikowski, W.; Sheng, Y. Nonlinear Talbot self-healing in periodically poled LiNbO<sub>3</sub> crystal [Invited]. *Chin. Opt. Lett.* **2021**, *19*, 060011. [[CrossRef](#)]
78. Chen, X.; Xu, C.; Liu, S.; Liu, D.; Tan, B.; Zhang, Y.; Chen, H.; Sheng, Y.; Wang, J. Influences of focusing conditions on optical poling in lithium niobate using a 1035 nm femtosecond fiber laser. *Appl. Opt.* **2023**, *62*, 6212–6217. [[CrossRef](#)]
79. Wang, X.; Cao, Q.; Wang, R.; Cao, X.; Liu, S. Manipulation of ferroelectric domain inversion and growth by optically induced 3D thermoelectric field in lithium niobate. *Appl. Phys. Lett.* **2022**, *121*, 181111. [[CrossRef](#)]

80. Imbrock, J.; Hanafi, H.; Ayoub, M.; Denz, C. Local domain inversion in MgO-doped lithium niobate by pyroelectric field-assisted femtosecond laser lithography. *Appl. Phys. Lett.* **2018**, *113*, 252901. [[CrossRef](#)]
81. Lisjikh, B.I.; Kosobokov, M.S.; Efimov, A.V.; Kuznetsov, D.K.; Shur, V.Y. Thermally assisted growth of bulk domains created by femtosecond laser in magnesium doped lithium niobate. *Ferroelectrics* **2023**, *604*, 46–51. [[CrossRef](#)]
82. Wang, X.; Cao, Q.; Wang, R.; Cao, X.; Liu, S. Domain growth driven by a femtosecond laser in lithium niobate crystal. *Opt. Lett.* **2023**, *48*, 566–569. [[CrossRef](#)] [[PubMed](#)]
83. Li, F.; Cao, Q.; Wang, X.; Wang, R. Nonlocal erasing and writing of ferroelectric domains using a femtosecond laser in lithium niobate. *Opt. Lett.* **2024**, *49*, 1892–1895. [[CrossRef](#)] [[PubMed](#)]
84. Liu, S.; Wang, L.; Mazur, L.M.; Switkowski, K.; Wang, B.; Chen, F.; Arie, A.; Krolikowski, W.; Sheng, Y. Highly Efficient 3D Nonlinear Photonic Crystals in Ferroelectrics. *Adv. Opt. Mater.* **2023**, *11*, 2300021. [[CrossRef](#)]
85. Hu, X.; Liu, S.; Xu, T.; Sheng, Y.; Zhao, R.; Krolikowski, W. Nonlinear generation of an optical bottle beam in domain-engineered ferroelectric crystals. *Opt. Lett.* **2023**, *48*, 5527–5530. [[CrossRef](#)] [[PubMed](#)]
86. Wang, S.; Liu, S.; Liu, D.; Wang, N.; Zhao, R.; Liu, Y.; Li, Z.; Mao, G.; Chen, F.; Sheng, Y.; et al. Ferroelectric domain engineering with femtosecond pulses of different wavelengths. *Opt. Express* **2023**, *31*, 5843–5852. [[CrossRef](#)] [[PubMed](#)]
87. Liu, X.; Tan, P.; Ma, X.; Wang, D.; Jin, X.; Liu, Y.; Xu, B.; Qiao, L.; Qiu, C.; Wang, B.; et al. Ferroelectric crystals with giant electro-optic property enabling ultracompact Q-switches. *Science* **2022**, *376*, 371–377. [[CrossRef](#)] [[PubMed](#)]
88. Chen, X.; Mazur, L.M.; Liu, D.; Liu, S.; Liu, X.; Xu, Z.; Wei, X.; Wang, J.; Sheng, Y.; Wei, Z.; et al. Quasi-phase matched second harmonic generation in a PMN-38PT crystal. *Opt. Lett.* **2022**, *47*, 2056–2059. [[CrossRef](#)] [[PubMed](#)]

**Disclaimer/Publisher’s Note:** The statements, opinions and data contained in all publications are solely those of the individual author(s) and contributor(s) and not of MDPI and/or the editor(s). MDPI and/or the editor(s) disclaim responsibility for any injury to people or property resulting from any ideas, methods, instructions or products referred to in the content.